Systems/Circuits

Physiological Diversity Influences Detection of Stimulus Envelope and Fine Structure in Neurons of the Medial Superior Olive

Brian J. Bondy,[1,2]* David B. Haimes,[1,2]* and Nace L. Golding[1,2]

[1]Department of Neuroscience, University of Texas at Austin, Austin, Texas 78712, and [2]Center for Learning and Memory, University of Texas at Austin, Austin, Texas 78712

The neurons of the medial superior olive (MSO) of mammals extract azimuthal information from the delays between sounds reaching the two ears [interaural time differences (ITDs)]. Traditionally, all models of sound localization have assumed that MSO neurons represent a single population of cells with specialized and homogeneous intrinsic and synaptic properties that enable the detection of synaptic coincidence on a timescale of tens to hundreds of microseconds. Here, using patch-clamp recordings from large populations of anatomically labeled neurons in brainstem slices from male and female Mongolian gerbils (*Meriones unguiculatus*), we show that MSO neurons are far more physiologically diverse than previously appreciated, with properties that depend regionally on cell position along the topographic map of frequency. Despite exhibiting a similar morphology, neurons in the MSO exhibit subthreshold oscillations of differing magnitudes that drive action potentials at rates between 100 and 800 Hz. These oscillations are driven primarily by voltage-gated sodium channels and are distinct from resonant properties derived from other active membrane properties. We show that graded differences in these and other physiological properties across the MSO neuron population enable the MSO to duplex the encoding of ITD information in both fast, submillisecond time-varying signals as well as in slower envelopes.

Key words: **AIS; binaural; coincidence detection; envelope coding; sound localization; superior olive**

Significance Statement

Neurons in the medial superior olive (MSO) encode sound localization cues by detecting microsecond differences in the arrival times of inputs from the left and right ears, and it has been assumed that this computation is made possible by highly stereotyped structural and physiological specializations. Here we report using a large (>400) sample size in which MSO neurons show a strikingly large continuum of functional properties despite exhibiting similar morphologies. We demonstrate that subthreshold oscillations mediated by voltage-gated Na^+ channels play a key role in conferring graded differences in firing properties. This functional diversity likely confers capabilities of processing both fast, submillisecond-scale synaptic activity (acoustic "fine structure"), and slow-rising envelope information that is found in amplitude-modulated sounds and speech patterns.

Introduction

Neurons of the medial superior olive (MSO) compare the arrival time of low-frequency sounds between two ears [interaural time differences (ITDs)], signaling the relative timing of binaural synaptic inputs with changes in firing rate (Goldberg and Brown, 1969; Yin and Chan, 1990). The MSO provides an especially clear example of a neural representation of a sensory feature, with neurons tuned to different ITDs representing discrete horizontal locations. Additionally, the MSO is a system where there is a strong relationship among circuitry, the biophysical properties of single cells, and a neural computation.

The original model for ITD tuning, the Jeffress model, postulated an array of identical neurons whose ITD and frequency tuning is based solely on their respective inputs (Jeffress, 1948),

Received Sep. 6, 2020; revised May 3, 2021; accepted May 5, 2021.

Author contributions: B.J.B., D.B.H., and N.L.G. designed research; B.J.B. and D.B.H. performed research; B.J.B., D.B.H., and N.L.G. analyzed data; B.J.B., D.B.H., and N.L.G. wrote the paper.

This work was supported by National Institutes of Health (NIH) Grants DC-006788 (N.L.G.) and F31-DC-016525, a Donald D. Harrington graduate fellowship (B.J.B), and NIH Grant F31-DC-017377 (D.B.H). We thank Dr. Matthew Rasband (Baylor College of Medicine) for providing immunolabeling advice and the antibodies to $Na_v1.6$ and AnkyrinG; Kenneth Ledford for assistance in writing code for data acquisition and analysis; and Dr. Michael Roberts for helpful discussions during early experiments, as well as collecting the phasic neuron *in vitro* ITD tuning data.

*B.J.B. and D.B.H. contributed equally to the work.

The authors declare no competing financial interests.

Correspondence should be addressed to Nace L. Golding at golding@austin.utexas.edu.

https://doi.org/10.1523/JNEUROSCI.2354-20.2021

and where systematic variations in axon length impart sensitivity to ITDs. The Jeffress model well describes the computation of the avian analog of the MSO, the nucleus laminaris (NL; Carr and Konishi, 1988; Carr et al., 2015). However, the NL deviates from the Jeffress model in that there are striking differences in intrinsic electrical properties along the tonotopic axis of the nucleus that have been proposed to aid effective neural coding over different frequency ranges. These gradients include intrinsic electrical properties (Koppl, 1994; Fukui and Ohmori, 2004; Wang et al., 2017) as well as dendritic (Smith and Rubel, 1979; Sanes et al., 1990) and axon initial segment (AIS) morphology (Kuba et al., 2005; Kuba, 2012).

The Jeffress model does not appear to describe ITD processing in the mammalian MSO nearly as well as in its avian counterpart. Axonal labeling has revealed a lack of systematic axonal delay lines from the cochlear nucleus to the MSO (Karino et al., 2011), leading to the postulation of several other sources of internal delay (Brand et al., 2002; Joris and Yin, 2007). Evidence for a systematic map of ITD tuning is likewise weak (Yin and Chan, 1990), and evidence for tonotopic gradients of neuronal properties in the MSO, akin to those seen in the NL has been conflicting (Scott et al., 2007; Baumann et al., 2013). A further complication in the mammalian circuitry is the presence of so-called "non-principal" neurons in the MSO, defined mostly on the basis of anatomic criteria (Stotler, 1953; Scheibel and Scheibel, 1974; Henkel and Spangler, 1983). What little data exist on the physiology of these cells suggest that they are less temporally precise than principal neurons (Smith, 1995; Chirila et al., 2007). These cells have not been incorporated in any model of MSO processing.

Here, we have examined electrophysiological and anatomic features of cells in the gerbil MSO, with special emphasis on extensive sampling and localization along its three-dimensional volume. Our data reveal a surprising and previously undescribed heterogeneity of intrinsic membrane and firing properties. Physiologic and morphologic features of MSO neurons do not define distinct "cell types," but instead create a continuous spectrum of response characteristics that may enhance the detection and encoding of information of sounds with a broad range of rise times and other temporal features.

Materials and Methods

All procedures were conducted in accordance with the Institutional Animal Care and Use Committee at The University of Texas at Austin (UT-Austin), following guidelines of the National Institutes of Health. Mongolian gerbils (*Meriones unguiculatus*) were raised in a colony at the UT-Austin Animal Resource Center and maintained on a 50 d/night cycle with continual access to food and water.

Brain slice preparation. Approximately equal numbers of both male and female Mongolian gerbils (45% males and 55% females of 330 animals that were documented) were anesthetized with isoflurane then decapitated after reflexes had ceased. Brains were removed in artificial CSF (ACSF) and a coronal blocking cut was made midway through the superior colliculus. For gerbils age postnatal day 18 (P18) to P22, all steps were conducted in ACSF warmed to 35°C, containing the following: 125 mM NaCl, 25 mM D-glucose, 2.5 mM KCl, 25 mM $NaHCO_3$, 1.25 mM NaH_2PO_4, 1.5 mM $MgSO_4$, 1.5 mM $CaCl_2$, pH adjusted to 7.45 with NaOH, and final osmolarity at 315 mOsm. Slices were cut at 200 µm thickness, incubated in ACSF at 35°C for 30–45 min, and then cooled to room temperature for >30 min. Slicing typically produced six to eight slices containing MSO. Following the preparation of slices, the sections immediately preceding and following the MSO were fixed for later reconstruction of the boundaries of the nucleus. ACSF for dissections and recordings was bubbled continuously with 95% O_2/5% CO_2. Dissections for gerbils older than P22 were conducted at room temperature. Following isoflurane anesthesia, gerbils were perfused and subsequently sectioned in a Na^+-free solution containing the following: 135 mM *N*-methyl-D-glucamine (NMDG), 20 mM D-glucose, 1.25 mM KCl, 1.25 mM KH_2PO_4, 2.5 mM $MgSO_4$, 0.5 mM $CaCl_2$, and 20 mM choline bicarbonate, pH adjusted to 7.45 using NMDG powder, and a final osmolarity of 310 mOsm. Slices were incubated at 35°C in the following recovery solution: 110 mM NaCl, 25 mM D-glucose, 2.5 mM KCl, 25 mM $NaHCO_3$, 1.25 mM NaH_2PO_4, 1.5 mM $MgSO_4$, 1.5 mM $CaCl_2$, 5 mM *N*-acetyl-L-cystine, 5 mM sodium ascorbate, 3 mM sodium pyruvate, and 2 mM thiourea, pH adjusted to 7.45 with NaOH, and a final osmolarity of 310 mOsm) for 30–45 min, then moved to room temperature for >30 min before recording.

Electrophysiology. Whole-cell current-clamp recordings were made using amplifiers (model BVC-700A, Dagan). Membrane voltage was filtered at 5 kHz, digitized at 50–100 kHz, and acquired using custom algorithms in IgorPro (WaveMetrics). Recording electrodes were pulled from thick-walled borosilicate glass (outer diameter 1.5 mm; inner diameter, 0.86 mm; 4–8 MΩ) and filled with an intracellular solution containing the following: 115 mM K-gluconate, 4.42 mM KCl, 0.5 mM EGTA, 10 mM HEPES, 10 mM, Na_2phosphocreatine, 4 mM MgATP, and 0.3 mM NaGTP, osmolality adjusted to 300 mOsm/L with sucrose, and pH adjusted to 7.30 with KOH. Biocytin (0.1%) was added to allow for cell labeling. All membrane potentials shown in this article are corrected for a 10 mV junction potential. Bridge balance and capacitance compensation were monitored in all recordings. All recordings were conducted at 35°C with oxygenated ACSF perfused at a rate of ~2–4 ml/min.

Data analyses for electrophysiology. Measurements of action potential (AP) shapes were made at rheobase. Rheobase spikes were acquired by finding a current step amplitude that would evoke an AP ~50% of the time. In most cases, at least 25 spikes were collected for analysis. *In vitro* ITD experiments were conducted using custom code written in IGOR-Pro (WaveMetrics) using methods described previously (Roberts et al., 2013). Bilateral synaptic stimuli with different timing offsets were presented randomly and were interleaved with unilateral stimuli and current steps (input resistance measurements). Synaptic stimulation was performed using a constant current stimulator (model DS3, Digitimer) and glass electrodes with 50–100 µm tips placed on the near the lateral nucleus of the trapezoid body (LNTB) for ipsilateral inhibitory stimulation, or near the center of the medial nucleus of the trapezoid body (MNTB) for contralateral inhibitory stimulation. Excitatory and inhibitory responses were isolated by adding 1 µM strychnine or 10 µM NBQX to the ACSF, respectively. Stimulation strength was adjusted so that ipsilateral and contralateral evoked EPSPs were approximately equal in amplitude. Stimulation intensity was also adjusted so that AP probability at the best timing offset was close to, but less than, 100%, to avoid saturation. *In vitro* ITD curves were normalized to maximal firing probability. Since stimulus-driven synaptic delays were dependent on electrode placement and thus arbitrary, the *x*-axes of ITD curves were offset so that maximal firing probability was 0 ms ITD. To obtain averaged ITD curves from experiments where different offset intervals were used, all curves were resampled to a common timescale in 0.05 ms increments using a linear interpolation.

Fast Fourier transforms (FFTs) were conducted in IGOR to measure the frequency of membrane oscillations. The average voltage was used to plot the FFT versus membrane potential. Heatmaps were generated in MATLAB and smoothed by interpolating points at 1 Hz intervals, and at intervals one-tenth of the existing voltage steps. Plots in the frequency domain were created by measuring the FFT of cell voltages depolarized to 2–7 mV below the AP threshold of the cell, typically over a window of 60 ms. Some tonic neurons required larger windows because of the slower oscillations, in which case voltage in the frequency domain was normalized to account for the extra time. For measurements of the change in voltage frequency with drug application (see Fig. 7*F*), voltage in the frequency domain was measured by integrating the values of the FFT in a 100 Hz window around the peak frequency. In other experiments, resonance frequency was measured from the peak of the impedance versus time plot calculated from the voltage responses to a chirp current injection (peak depolarization, ~5 mV; 10 s long at –60 mV).

The frequency of the chirp increased linearly from 0 to a maximum value that was adjusted so that the resonant frequency occurred near the middle of the chirp.

Principal component analysis (PCA), and group analyses were performed in Rstudio (R version 4.0.4). Briefly, 31 features were chosen for PCA, 12 electrophysiological and 19 morphologic. Separate datasets were constructed for each feature and subjected to MICE (Multiple Imputation by Chained Equations) imputation to account for occasional missing measurements in some cells (MICE version 3.11.0; van Buuren and Groothuis-Oudshoorn, 2001). Briefly, MICE imputation involves estimating missing data by performing linear regression on existing data and then predicting possible values. Multiple datasets are generated from these possible values, with pooling of these results leading to a single, final dataset. Data were centered and scaled with principal component analysis (stats version 3.6.3) and visualized (factoextra versioin 1.0.7).

Immunostaining. Following isoflurane anesthesia, the brainstems of Mongolian gerbils (age range, P22 to P28) were rapidly removed and drop fixed for 30–60 min in ice-cold 4% paraformaldehyde (PFA). Brains were transferred to 20% sucrose (in 0.1 M PBS) overnight at 4°C, followed by a second night in 30% sucrose. The tissue was sectioned on a cryostat at 20–35 μm, then transferred to 0.1 M PBS, mounted and dehydrated. For immunohistochemistry, slides were rehydrated in 0.1 M PBS for 10–15 min and covered with phosphate buffer/Triton/goat serum blocking solution (PBTGS; 10% goat serum, 0.3% Triton in 0.1 M PBS) for 1.5 h. The tissue was incubated (24–48 h 4°C) with PBTGS containing mouse anti-HCN1 (1:200; NeuroMab) and either 1:100 rabbit anti-$Na_v1.6$ or 1:200 rabbit anti-AnkyrinG (courtesy of Matthew Rasband, Baylor College of Medicine, Houston, TX). After primary incubation, the tissue was gently washed 3× with 0.1 M PBS (5, 10, and 15 min intervals) at room temperature and then incubated for 2 h with PBTGS containing 1:250 goat anti-mouse Alexa Fluor 568 (1:250; Abcam) and goat anti-rabbit Cy2 (1:250; The Jackson Laboratory). Following secondary incubation, tissue was again washed 3× with 0.1 M PBS. The third wash (15 min) was performed in 0.05 M PBS, dried, and coverslipped with Fluoromount-G (Thermo Fisher Scientific).

Imaging. Images were taken on a laser-scanning confocal microscope (model TCS SP5 II, Leica). Large images of the entire MSO were taken using tile scanning and *z*-stacks with an average of 0.7 μm thin optical sections. Image parameters were set to provide subsaturation of pixels in the axon initial segment. Fluorescence was excited by 488 and 543 nm lasers. Images were then reconstructed on Neurolucida 360, and AnkyrinG-positive AISs were demarcated by 20% maximal fluorescence cutoffs at the proximal and distal ends. Linear pixel plots, also known as intensity profiles (spatial distribution of pixel intensities within an image), were generated using a rolling average across the width of the AIS to help determine cutoffs. Measurements were also made between the axon emergence point on the soma or proximal dendrite, and the start of the fluorescent signal at the proximal end of the AIS. Data from each individual tracing was plotted against relative location across the dorsal–ventral axis of the MSO.

Histology. To determine the precise ventral–dorsal position of each recorded neuron, cells were labeled by including 0.1% biocytin in the internal solution and postexperimental processing. Following each recording, the MSO and pipette location were either sketched under low power or imaged directly, after which the brain slices were stored in 4% PFA for 24–48 h before being switched to a 1× PBS solution. Biocytin staining on 200 μm slices was performed using ABC and DAB staining kits from Vector Laboratories, and processing was conducted according to the manufacturer instructions. Slices were mounted on slides using Mowiol mounting agent. Coverslips were sealed using nail polish after drying. Cells were reconstructed using a 100× objective, and the superior olivary complex (SOC) as well as other brain nuclei were traced using 4× or 10× objectives (model BX51 Light Microscope, Olympus) using Neurolucida software. Truncated dendritic arbors were excluded unless the ending occurred >100 μm from the soma. Low-power drawings of slices, together with measurements of ventral–dorsal location, were used to determine the identity of cells after biocytin staining was performed in the event that not all recorded cells were labeled properly. Biocytin staining typically produced a clear background labeling of the SOC nuclei, which was used to create a rough outline of the MSO under low power. Subsequently, ventral and dorsal ends of this outline were investigated under 100× magnification for any spindle-shaped cell bodies, which were traced. The absence of these spindle-shaped cell bodies was used as a further marker for the boundaries of the MSO, particularly for the dorsal end of the MSO. The ventral border of the MSO is marked by a large fiber tract that separates the MSO from the ventral nucleus of the trapezoid body (VNTB), and often provided a very clear border. Thus, a combination of these fiber tracts, the locations of the lateral superior olive (LSO) and VNTB, and the locations of spindle-shaped neurons were used to determine the boundaries of the MSO. Since the ventral–dorsal length of the MSO varies along its rostral–caudal axis, ventral dorsal position is expressed as the position of a cell along the normalized length of the MSO within a given slice. Any cell found to be outside of the marked region was excluded from all analyses.

Statistics. In all experiments, values are presented as the mean ± SEM, and statistical significance was assessed using a nonparametric ANOVA (Kruskal–Wallis test) across the three firing types. Subsequent pairwise comparisons were performed using a two-sided Wilcoxon test. *p* Values with no test specified are from the Wilcoxon test. Effect size is reported as a Hedges's *g* value. Significance level was set at 0.05. Normality of distributions was not assumed. Numbers of replications of experiments are equal to the number of cells recorded/analyzed.

Data availability. The data are available at https://github.com/dhaimes-b/MSO_CellType_Diversity (commit f143e96).

Results

To assess whether there are topographic differences in the physiology or morphology of MSO neurons, we made whole-cell recordings from 422 MSO neurons in coronal brainstem slices from gerbils with an age range of postnatal day 18 (P18) to P68, and subsequently localized labeled neurons within the three dimensions of the nucleus through biocytin staining. Up to nine neurons were recorded across the tonotopic (ventral–dorsal) axis in a single slice, and as many as 16 cells could be recorded across multiple slices from a single gerbil. Of the group of coronal slices, 337 were labeled well enough to localize within the MSO, and 270 of these neurons could be reconstructed fully. A further 72 cells recorded in horizontal slices were included in this study, but cell location data were not collected for these neurons.

MSO neurons have a continuum of diverse physiological properties

In our experiments, we observed a diversity in physiology and morphology not previously reported. We observed three general patterns of firing in response to step injections of current, although there was no discrete boundary between firing types. Figure 1*A* shows two examples from each group of neurons. A total of 63% of cells displayed properties consistent with previous reports from MSO principal neurons, which we term "phasic neurons": a single AP in response to intracellularly injected current steps, a single-phase afterhyperpolarization (AHP), a fast membrane time constant [phasic ($n = 292$): $\tau_m = 0.319 \pm 0.005$ ms], and low input resistance [phasic ($n = 292$): 10.5 ± 0.2 MΩ; Fig. 1*A*,*B*,*E*, black traces or points]. We also observed a subset of neurons that fired repetitively, which we separated into two groups based on the pattern and shape of their APs, the "oscillator neurons" and "tonic neurons."

Oscillator neurons ($n = 97$) fired high-frequency AP trains at the beginning of the response to steps of current, followed by a period of silence marked by large, high-frequency subthreshold oscillations (Fig. 1*A*,*C*, blue traces). In approximately half of oscillator neurons these oscillations gave way to high-frequency spiking during responses to larger-amplitude steps, with each AP

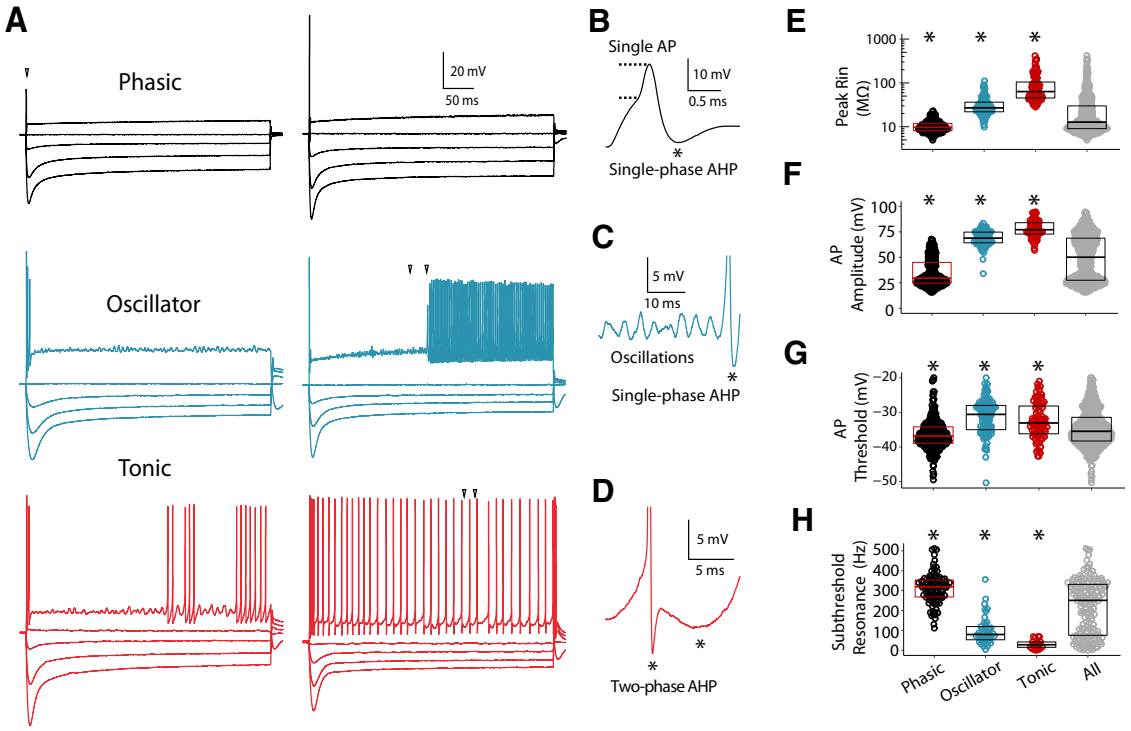

Figure 1. MSO principal neurons exhibit a spectrum of membrane properties and firing types. ***A***, Six examples of MSO neurons, sorted into three categories. Arrows indicate features displayed in ***B–D***. Top, Phasic neurons with small and large APs (left and right, respectively). Middle, Oscillator neurons with onset-only APs (left) and gap firing (right). Bottom, Tonic neurons displaying patterns of gap (left) and regular firing (right). ***B–D***, Distinguishing features of each category, with one-phase or two-phase AHPs, marked by asterisks. ***B***, Phasic neurons fire only one AP with a single-phase AHP in response to current steps. Dashed lines indicate AP threshold and peak voltage. ***C***, Oscillators fire multiple APs (each with single-phase AHPs) and exhibit large, high-frequency subthreshold oscillations, which may evolve into high-frequency spiking. ***D***, Tonic neurons show repetitive firing patterns and APs exhibiting two-phase AHPs. ***E–H***, Scatter dot plots comparing electrophysiological properties of the three firing types as well as the merged dataset ("All"). Box plots show first and third quartiles centered around the mean. Nonparametric statistics: Kruskal–Wallis test for overall differences in the population. Individual group means were then compared against the mean of all groups together with a Wilcoxon test (*$p < 0.001$). ***E***, Peak input resistance (log scale), measured from the lowest point of the hyperpolarized portion of the *I–V* curve. Kruskal–Wallis test, $p = 8.37e\text{-}67$; Wilcoxon test: phasic, $p = 1.75e\text{-}16$; oscillator, $p = 4.03e\text{-}11$; tonic, $p = 3.56e\text{-}28$. ***F***, AP amplitude (from AP threshold to AP peak). Kruskal–Wallis test, $p = 5.03e\text{-}68$; Wilcoxon test: phasic, $p = 1.11e\text{-}17$; oscillator, $p = 5.37e\text{-}14$; tonic, $p = 1.21e\text{-}24$. ***G***, Absolute threshold, measured at the point where dV/dt = 40 mV/s. Kruskal–Wallis test, $p = 1.38e\text{-}20$; Wilcoxon test: phasic, $p = 3.04e\text{-}6$; oscillator, $p = 2.39e\text{-}9$; tonic, $p = 8.60e\text{-}4$. ***H***, Resonance frequency, measured as the peak impedance from a 10 s chirp stimulus. Kruskal–Wallis test, $p = 3.49e\text{-}24$; Wilcoxon test: phasic, $p = 4.84e\text{-}7$; oscillator, $p = 4.07e\text{-}6$; tonic, $p = 2.05e\text{-}9$.

displaying a single-phase AHP. Any neuron that fired more than one AP in response to a current step was considered an oscillator neuron, unless it fit the criteria of a tonic neuron (see below). Oscillator neurons exhibited input resistances and time constants three to five times larger than those of phasic neurons [input resistance (R_{in}): 34.6 ± 2.69 MΩ; $n = 101$; τ_m: 0.94 ± 0.09 ms; $n = 74$; Fig. 1*E*]. APs in oscillator neurons were larger than those in phasic neurons [oscillator ($n = 95$): 68.3 ± 0.8 mV vs phasic ($n = 253$): 34.9 ± 0.8 mV, $p = 6.27e\text{-}45$, $g = 2.79$; Fig. 1*F*], and exhibited a relatively higher voltage threshold for initiation [oscillator ($n = 95$), −40.9 ± 0.7 mV; vs phasic ($n = 248$), −46.5 ± 0.3 mV; $p = 3.57e\text{-}18$, $g = 1.12$, Fig. 1*G*] despite a smaller rheobase [oscillator ($n = 95$), 585 ± 20 pA; vs phasic ($n = 253$), 1991 ± 48 pA; $n = 253$, $p = 2.97e\text{-}47$, $g = 2.22$]. Finally, in response to subthreshold chirp stimuli (peak depolarization, ~5 mV; 10 s long; see Materials and Methods), oscillator neurons displayed maximal resonance at a lower frequency than phasic neurons [oscillator ($n = 42$), 100 Hz; vs phasic ($n = 97$), 310 Hz; $p = 4.61e\text{-}18$, $g = 2.77$; Fig. 1*H*].

Tonic neurons ($n = 68$) fired more regularly and at lower frequency in response to current steps compared with oscillators (Fig. 1, red vs blue traces), and individual APs exhibited a distinctive two-phase AHP (Fig. 1*D*). Any MSO neuron that fired repetitively and displayed a two-phase AHP was considered a tonic neuron. Tonic neurons ($n = 50$) exhibited input resistances and time constants threefold to fivefold higher than those of oscillator neurons (R_{in}: 102.4 ± 10.5 MΩ, $p = 1.40e\text{-}20$, $g = 1.15$; τ_m: 4.38 ± 072 ms, $p = 3.26e\text{-}13$, $g = 1.04$; Fig. 1*E*). AP threshold in tonic neurons was also elevated compared with phasic neurons [tonic ($n = 65$): −42.4 ± 0.66 mV, $p = 2.22e\text{-}9$, g = 0.85], despite far lower rheobase currents [tonic ($n = 65$): 287 ± 22 vs 1991 ± 48 pA, $p = 6.34e\text{-}41$, $g = 2.53$], and were also significantly different from the threshold of oscillator neurons ($p = 8.22e\text{-}18$, $g = 1.62$; Fig. 1*G*). While oscillator neurons had a similar resting potential (V_{rest}) compared with phasic neurons [oscillator ($n = 95$): −60.2 ± 0.4 mV, $n = 100$; vs phasic ($n = 253$): −59.1 ± 0.19 mV, $p = 1.41e\text{-}2$; $g = 0.38$], V_{rest} in tonic neurons was more negative [tonic ($n = 65$), −65.5 ± 0.72 mV; tonic vs oscillator, $p = 2.98e\text{-}9$, $g = 1.03$; tonic vs phasic, $p = 1.35e\text{-}19$, $g = 1.64$]. These differences in V_{rest} further accentuated the differences in AP threshold relative to rest [phasic ($n = 253$), 12.7 ± 0.23 mV; oscillator ($n = 95$), 19.1 ± 0.48 mV; tonic ($n = 65$), 23.1 ± 0.64 mV; Kruskal-Wallis test, $p = 3.08e\text{-}47$; phasic vs oscillator, $g = 1.63$; phasic vs tonic, $g = 2.57$; oscillator vs tonic, $g = 0.77$].

While many physiological parameters showed systematic differences in properties across firing types, there was a high degree of overlap in values (Fig. 1*E–H*, all category). Neurons with intermediate properties were common. Oscillators without late APs tended to have properties more similar to phasic neurons. Many

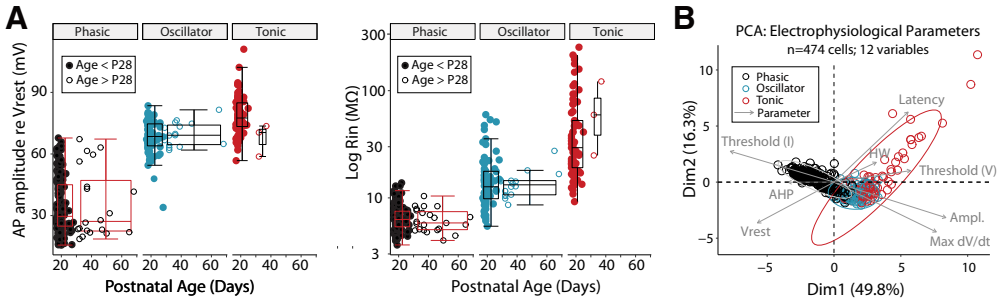

Figure 2. MSO principal neurons exhibit a continuum of electrophysiological properties that persists at older ages. ***A***, AP amplitude and R_{in} in cells from animals between P28 and P68 (open circles) span a range of values similar to those from animals between P18 and P28 (closed circles). Data split according to cell-firing type. Statistics were not performed because of uneven numbers of neurons in the age categories shown. ***B***, PCA of electrophysiological parameters ($n = 474$ cells; 12 features; recordings from all ages), from an imputed dataset (MICE). Highly impactful features are shown with gray arrows, with the length corresponding to vector strength in principal component analysis space.

phasic neurons displayed overshooting APs (Fig. 1*A*, right example), and some displayed noticeable subthreshold oscillations (data not shown).

While the majority of the neurons in this dataset were recorded at P18 to P28 (phasic, $n = 250$; oscillator, $n = 81$; tonic, $n = 65$), all of these firing phenotypes were observed in older animals between P28 and P68, when both morphologic and physiological features of MSO neurons have reached stability (Rautenberg et al., 2009; Mathews et al., 2010; Khurana et al., 2012; phasic, $n = 23$; oscillator, $n = 16$; tonic, $n = 3$). We found that electrophysiological features from this older age range fell within the range of values observed in animals from age P18 to P28 (e.g., first/third quartiles, mean; Fig. 2*A*), although the large imbalances in sample sizes precluded formal statistical comparisons. When cells with phasic, oscillating, and tonic firing patterns were compared using PCA of 12 primary electrophysiological parameters, the distributions were overlapping and formed a bimodal continuum (Fig. 2*B*). Thus, electrophysiological criteria alone do not support phasic, oscillator, and tonic neurons as distinct cell types within the MSO neuron population.

All MSO neurons are principal neurons

Figure 3*A–D* illustrates four example brainstem slices with reconstructed neurons. The yellow spindle shapes are nonlabeled cell bodies that were marked under 100× magnification to aid in demarcating the boundaries of the MSO (see Materials and Methods). As with phasic neurons, oscillator and tonic neurons were located in the main column of cell bodies. In two cases, neurons were recorded outside of the cell body layer and in the indistinct territory between the MSO and neighboring nuclei like the LNTB. These cells were morphologically and physiologically distinct from the neurons described here and were not included in our analyses. While some dorsal oscillator and tonic neurons did not display an obvious bipolar dendritic architecture (Fig. 3*B*, red cell), most cells displayed morphologies that have been described previously. Phasic neurons ($n = 220$) were generally located throughout the nucleus, while oscillator and tonic neurons (oscillator, $n = 84$; tonic, $n = 65$) tended to be biased toward the dorsal and ventral ends of the nucleus (Fig. 3*E*). Furthermore, two cells with different firing types could be recorded directly adjacent to each other (Fig. 3*A*,*D*), and all three firing types could be recorded in the same slice (Fig. 3*A*).

The axons of phasic MSO neurons typically traveled dorsally, passing either between the superior periolivary nucleus (SPN) and the LSO or through the SPN, en route to the inferior colliculus (Fig. 3*A–D*, black neurons). The axons of oscillator and tonic neurons (Fig. 3*A–D*, blue and red neurons) took a similar path. Many phasic neuron axons took a roundabout path out of the nucleus, often traveling ventral for some distance before turning dorsal (Fig. 3*C*, topmost neuron, *D*, most ventral phasic neuron). This pattern was also seen in oscillator neurons (Fig. 3*A*,*C*) and tonic neurons (data not shown). As with phasic neurons, axons of oscillator and tonic neurons frequently sent local collaterals within the MSO, as well as collaterals in the SPN. All MSO neurons projected outside of the nucleus, indicating that there were no pure interneurons/non-principal neurons in the MSO. There were no axons that could be traced dorsal to the LSO (Fig. 3*B*).

Dendritic morphology is a poor indicator of firing type

Although prior studies have highlighted the presence of discrete morphologic cell types in the MSO (Stotler, 1953; Scheibel and Scheibel, 1974; Henkel and Spangler, 1983); quantitative analyses of 270 biocytin-labeled neurons revealed that dendritic morphology can vary across MSO neurons, and is an imperfect indicator of firing type (Fig. 4*A–D*). Most MSO neurons exhibited a bipolar architecture with a similar pattern of tapering, dendritic length, and general complexity. It was observed that a small number of oscillator and tonic neurons with longer dendritic arbors were present, particularly at the dorsal end of the nucleus, although many of these were excluded from analyses because of incomplete dendritic arbors. Overall, however, there were no systematic differences in anatomic parameters along the tonotopic axis (mean dendritic length: phasic, $R^2 = 0.013$; oscillator, $R^2 = 0.130$; tonic, $R^2 = 0.028$; number of branch points: phasic, $R^2 = 0.016$; oscillator, $R^2 = 0.001$; tonic, $R^2 = 3e\text{-}04$; Fig. 4*B*,*C*). Principal component analysis on imputed data (see Materials and Methods; $n = 223$ cells; 19 features) showed a strong overlap of each firing type with solely morphologic features (data not shown, but available at https://github.com/dhaimes-b/MSO_CellType_Diversity). Combining these morphologic features with the electrophysiological features (Fig. 2*B*) produced slightly more group separation in principal component analysis ($n = 200$ cells; 31 features: 12 electrophysiological, 19 morphologic), although strong overlap still existed (Fig. 4*D*). Together, the anatomic results indicate that there are no strong trends in morphology along the tonotopic axis, and overall the data do not support the existence of separable anatomic cell types.

Oscillator and tonic neurons have slower synaptic kinetics

MSO neurons from all three firing types received bilateral excitation (Fig. 5*A*). Electrical stimulation of bushy cell axons from the cochlear nucleus evoked EPSPs that were widest in tonic neurons, and narrowest in phasic neurons [half-width: phasic ($n = 14$), 0.52 ± 0.015 ms; oscillator ($n = 14$), 1.42 ± 0.21 ms;

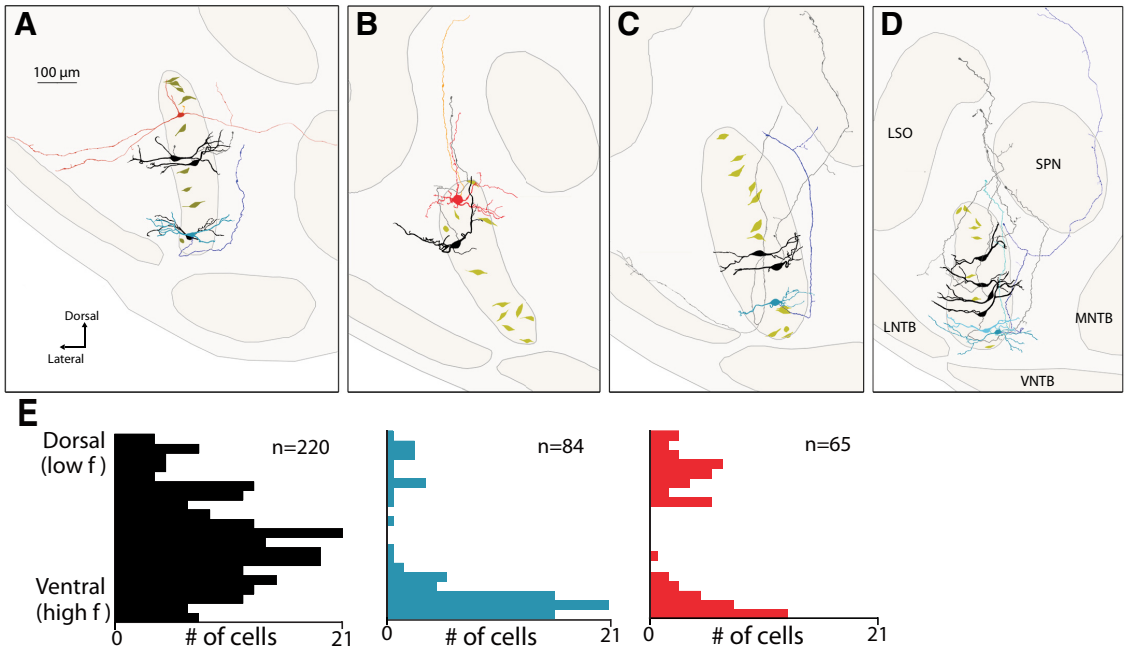

Figure 3. MSO neurons of all firing types send long-distance projections with similar trajectories. ***A–D***, Phasic neurons, Black, with gray axons; tonic neurons, red, with orange axons; oscillators, blue, with dark blue axons. The two oscillator neurons and their axons in ***D*** are colored in different shades to better differentiate them. Dark yellow shapes are spindle-shaped cell bodies of unlabeled neurons to help delineate the boundaries of the MSO. Nuclei labeled in ***D*** apply to all panels. ***E***, Distributions of recorded cells along the tonotopic axis of the MSO, normalized according to dorsal (low-frequency) and ventral (high-frequency) borders.

tonic ($n = 6$), 3.74 ± 0.77 ms; Kruskal–Wallis test, $p = 1.1e\text{-}05$; Wilcoxon test: phasic vs oscillator, $p = 5.6e\text{-}05$; phasic vs tonic, $p = 2.1e\text{-}4$; oscillator vs tonic, $p = 4.0e\text{-}05$]. The kinetics of EPSPs strongly influenced the sensitivity of a given neuron to the coincidence of bilaterally evoked synaptic input (Fig. 5*A*). Oscillator and tonic neurons more readily summed inputs with larger timing offsets. Few phasic neurons fired APs in responses to timing offsets >0.5 ms. By contrast, every tonic neuron recorded could fire in response to time differences >1 ms, with one neuron firing to time differences as large at 5 ms. The slopes of these *in vitro* ITD tuning curves were 2.5-fold and sevenfold steeper in phasic neurons relative to oscillator and tonic neurons, respectively (Fig. 5*B*,*C*: slope of sigmoid fit: phasic neurons, 0.056 ± 0.004 ms; oscillator neurons, 0.135 ± 0.019 ms; tonic neurons, 0.41 ± 0.17 ms). ITD functions were narrowest in phasic neurons and widest in tonic neurons (Fig. 5*B*,*D*), and ITD width was highly correlated with input resistance (Fig. 5*E*; linear regression: $F_{(1,30)} = 83.51$, $p = 3.57e\text{-}10$, $R^2 = 0.86$,).

Axon initial segment morphology is uniform across the MSO

The AIS possesses a high density of voltage-gated Na and K channels and is typically the site of spike generation. Thus, variations in AIS length, diameter, and proximity to the soma could potentially contribute to the different spike thresholds and firing patterns observed across MSO cells. To determine whether the AIS varies with functional firing phenotypes, we quantified AIS morphology as a function of tonotopic location in the MSO in fixed coronal sections of the MSO (Fig. 6). Dual immunolabeling of the AIS marker AnkyrinG and hyperpolarization-activated cyclic nucleotide-gated (HCN) channels (the latter to visualize the soma), revealed that the AIS was highly uniform along the tonotopic axis both in its length (17.8 ± 0.1 µm, $n = 833$) as well as its starting location in the axon with respect to edge of the soma (<0.2 ± 0.012 µm; Fig. 6*A*,*C*,*E–G*). Further, dual immunolabeling with antibodies to $Na_v1.6$ and HCN1 subunits showed that $Na_v1.6$ was not present in the most proximal portion of the AIS, consistent with a prior study (Fig. 6*B*,*D*; Ko et al., 2016). This proximal spacer in the $Na_v1.6$ signal and the total length of the $Na_v1.6$ segment were also uniform across the tonotopic axis (Fig. 6*E–G*).

Subthreshold voltage oscillations are mediated by fast Na^+ channels

Subthreshold oscillations were a feature of all MSO neurons regardless of firing pattern but differed in amplitude and frequency (Fig. 7). Oscillations in phasic neurons were small (<1 mV) and high in frequency (400–800 Hz; Fig. 7*A*, black traces), whereas in both oscillator and tonic neurons oscillations were far more prominent (Fig. 7*A*, blue and red traces). In tonic neurons, oscillations were often difficult to visualize because they occurred only over a narrow range of voltages just below AP threshold. Spectral analyses of oscillations at different membrane potentials showed that oscillation frequency increases with the square of membrane potential monotonically, with all firing types forming a continuum (Fig. 7*B*,*C*). In tonic and oscillator neurons, subthreshold oscillations and firing frequency were distinctly correlated: this was most easily visualized in oscillator neurons, where subthreshold oscillations and AP trains of similar frequencies could be measured in individual responses (Fig. 7*D*). Finally, oscillations were eliminated by application of 1 µM tetrodotoxin (TTX) either to the bath or locally to the soma and axon (90–95% reduction in power; see Materials and Methods; Fig. 7*E*), indicating that oscillations were driven primarily by voltage-gated Na^+ channels, regardless of firing type.

Reduced slope sensitivity allows oscillator and tonic neurons to respond to amplitude-modulated-like stimuli

The striking differences in membrane and firing properties of MSO neurons raise the question of what functional significance

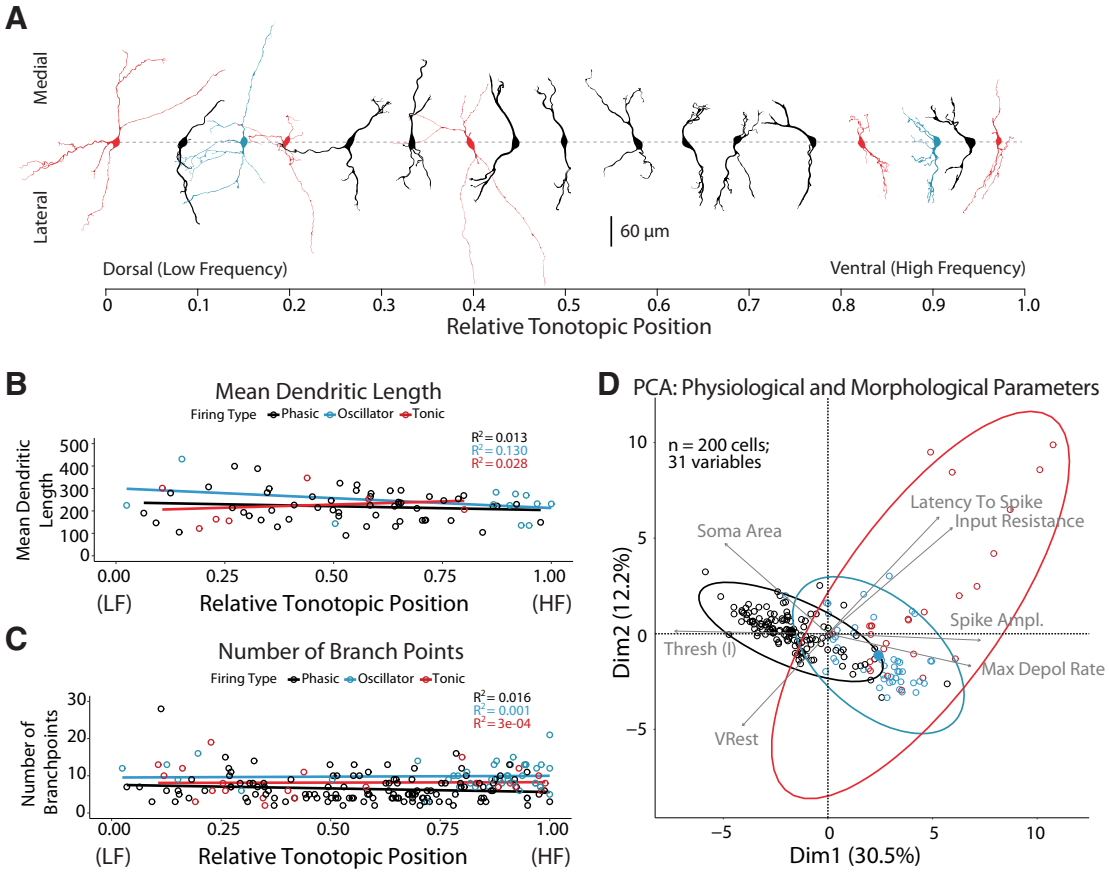

Figure 4. Morphologic parameters do not separate MSO principal neurons by firing types. ***A***, Example Neurolucida reconstructions of filled, recorded MSO cells, positioned by their normalized dorsal (low-frequency) to ventral (high-frequency) location. Neurons are false colored by recorded firing type. ***B***, ***C***, Reconstructed neurons were analyzed with Sholl analysis using Neurolucida. There were no strong correlations with morphologic parameters and tonotopic position within the nucleus for either mean dendritic length (***B***) or number of branch points (***C***). ***D***, PCA of 200 cells that were electrophysiologically characterized and subsequently processed for morphologic quantitation. A subset of 31 features (12 electrophysiology, 19 morphologic) were used to perform the principal component analysis. Vectors show a curated selection from the 15 strongest contributing features, with corresponding directionality and strength. Centroids of the ellipses are displayed as enlarged, filled circles.

such diversity may play in encoding binaural information, particularly in high-frequency regions of the MSO. One possibility is that such properties represent adaptations to detect low-frequency envelopes of high-frequency, amplitude-modulated (AM) sounds. To test this, we injected current into neurons in the shape of a fully rectified sine wave. This stimulus was designed to approximate the pattern of synaptic summation experienced by MSO neurons *in vivo* in response to AM sounds, based on known responses of bushy cells in the cochlear nucleus (Frisina et al., 1990). The frequency and amplitude of simulated envelopes were varied systematically to determine how different neurons responded to inputs that produced slow- or fast-rising voltage responses.

Phasic neurons showed markedly different responses to these simulated envelopes, compared with oscillator and tonic neurons (Fig. 8*A–C*). Phasic neurons typically would not fire in response to envelopes <100 Hz. Often, APs could not be evoked on the first several cycles of a 100 Hz envelope, regardless of current amplitude (up to 6.5 nA). The current threshold for evoking APs decreased as the frequency of the envelope increased up to 400–600 Hz. At higher frequencies, spiking became more difficult to evoke, likely because of depolarization block (Fig. 8*A*, elevated membrane potential, 1000 Hz phasic neuron).

Both tonic and oscillator neurons responded to simulated envelopes across a broad range of frequencies (Fig. 8*C*,*D*). In some oscillator neurons, firing thresholds became elevated at lower frequencies, with several neurons showing low-frequency cutoffs (Fig. 8*D*). Oscillator and tonic neurons differed dramatically from phasic neurons in their ability to fire multiple APs per cycle at envelope frequencies ≤200 Hz. In many cases, this resulted in oscillator and tonic neurons firing the same number of APs per second long-envelope stimulus, regardless of frequency (Fig. 8*C*, overlapping curves for tonic neuron). With the exception of the slowest tonic neurons, most MSO neurons could fire APs at the envelope frequency 1:1 for frequencies up to 600–800 Hz.

The characteristic subthreshold oscillations in oscillator neurons were particularly prominent during low-frequency envelope injections. Figure 8*B* shows an example response of an oscillator to a 10 Hz envelope at several current amplitudes. These oscillations reached peak amplitude at voltages close to threshold. At suprathreshold voltages, oscillations preceded spiking, could exceed 6 mV in amplitude, and typically drove subsequent repetitive spiking. Large oscillations were also seen in tonic neurons during envelope current injections, although in most cases the voltage range between the emergence of oscillations and spiking was narrow.

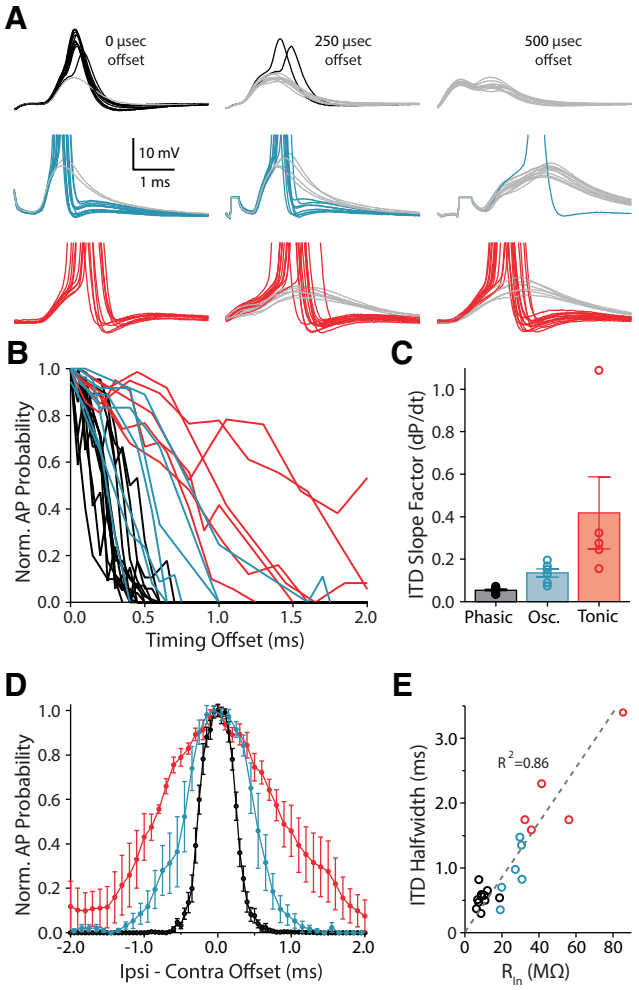

Figure 5. Diversity in temporal resolution across MSO neuron firing phenotypes. ***A***, Responses to bilateral synaptic excitation at different temporal offsets in phasic, oscillator, and tonic firing phenotypes (black, blue, and red traces, respectively). For each firing type, subthreshold responses are shown in gray. APs in oscillator and tonic neurons are truncated. ***B***, Spike probability versus timing offset. Only the right half of the ITD curve is shown for clarity. ***C***, Slope of sigmoidal fits of each side of ITD curves of neurons. Each point represents an average of the right-hand and left-hand slopes for each curve. Error bars represent ±SEM. ***D***, Averaged *in vitro* ITD tuning curves for each cell type. ***E***, Correlation between the half-width of ITD curves and neuronal input resistance. Dashed line: linear fit to the data points [$y = 0.045\times + 0.1$], with the R^2 value given in the figure (0.86).

Discussion

Traditionally, the binaural neurons of the MSO have been assumed to comprise a highly stereotyped cell type, with submillisecond membrane properties, transient firing pattern, and bipolar dendritic morphology. Here, we show in a large sample of neurons and detailed mapping of subnucleus location that the functional properties of MSO neurons are strikingly variable, and that a substantial proportion of neurons in the MSO exhibits functional properties incompatible with the classic model of MSO processing. Specifically, subsets of MSO neurons show slower membrane properties as well as high-frequency firing driven by subthreshold voltage oscillations. While MSO neurons can be grouped into descriptive categories based on firing pattern, we found no compelling evidence that these three categories represent fully separable cell types. We show that these disparate properties enable different MSO neurons to detect activity with vastly different rise times, ranging from submillisecond *in vitro* ITDs (the traditional role attributed to MSO neurons) to slower rising envelopes over hundreds of milliseconds. Thus, physiological diversity enables the population of MSO neurons to effectively process a wider range of acoustic stimuli than previously recognized.

The MSO contains a single cell type with variable physiological properties

Previous physiological studies in MSO neurons have defined two cell types in the MSO: the principal neurons, with bipolar dendrites, phasic firing, and fast membrane properties (Grothe and Sanes, 1994; Scott et al., 2005; Rautenberg et al., 2009); and the non-principal neurons, with stellate morphology, regular firing, and slower membrane properties (Henkel and Spangler, 1983; Smith, 1995; Chirila et al., 2007). While many of these prior observations were apparent in our recordings, more extensive sampling across the whole tonotopic range of the MSO suggests that these non-principal neurons are not fully distinct from principal neurons (Figs. 1, 2). Several lines of evidence support the concept that there is a single cell type in the MSO. The initial trajectories of the axonal projections of oscillator and tonic neurons were not different from those of phasic neurons (Fig. 3), showing qualitatively similar patterns in both projection path and collateral targets. Immunohistochemical studies have not shown the presence of neurons expressing glycine or GABA in the MSO, indicating that there are no inhibitory subpopulations (Roberts and Ribak, 1987; Wenthold et al., 1987). All firing types received qualitatively similar patterns of bilateral excitatory and inhibitory synaptic inputs: (Fig. 5, for excitatory inputs).

All firing types could be found at the ventral and dorsal extremes of the nucleus. However, only phasic neurons were seen in the center of the MSO. This trend persisted despite heavy sampling of the middle third of the MSO. The low prevalence of nonphasic neurons in the middle tonotopic range also may explain why nonphasic neurons have been rarely reported in studies of the MSO using horizontal slices, where sampling is likely biased to the middle tonotopic region of the nucleus (Scott et al., 2005; Khurana et al., 2011).

Heterogeneity in intrinsic electrical properties within neural circuits

The variability in properties of specific cell types has sometimes been treated as experimental noise, but theoretical studies have shown that such heterogeneity confers spiking output that carries higher information content (Padmanabhan and Urban, 2010; Tripathy et al., 2013). Neuronal variability can be the result of a topographic or regional gradient in properties, even outside of sensory and motor systems. Stellate neurons of the medial entorhinal cortex also appear to exhibit positional differences in HCN currents and leak K^+ currents that affect temporal summation, influencing their encoding of grid cell spacing (Garden et al., 2008; Giocomo et al., 2011). Gradients of ion channels along the tonotopic axis are a ubiquitous feature of the avian auditory system. Neurons in the nucleus laminaris display a striking gradient of dendritic morphology along the tonotopic axis (Smith and Rubel, 1979; Sanes et al., 1990) as well as many other features, which have been correlated with improved coding of low-frequency versus high-frequency sound information (Fukui and Ohmori, 2004; Kuba et al., 2005; Hong et al., 2018). There are several examples of similar gradients in mammalian auditory nuclei. In the LSO and MNTB, neurons in low-frequency regions fire transiently and express fast intrinsic membrane properties, in part reflecting a higher density of K^+ channels (Barnes-Davies et al., 2004; Brew and Forsythe, 2005). In both avian and

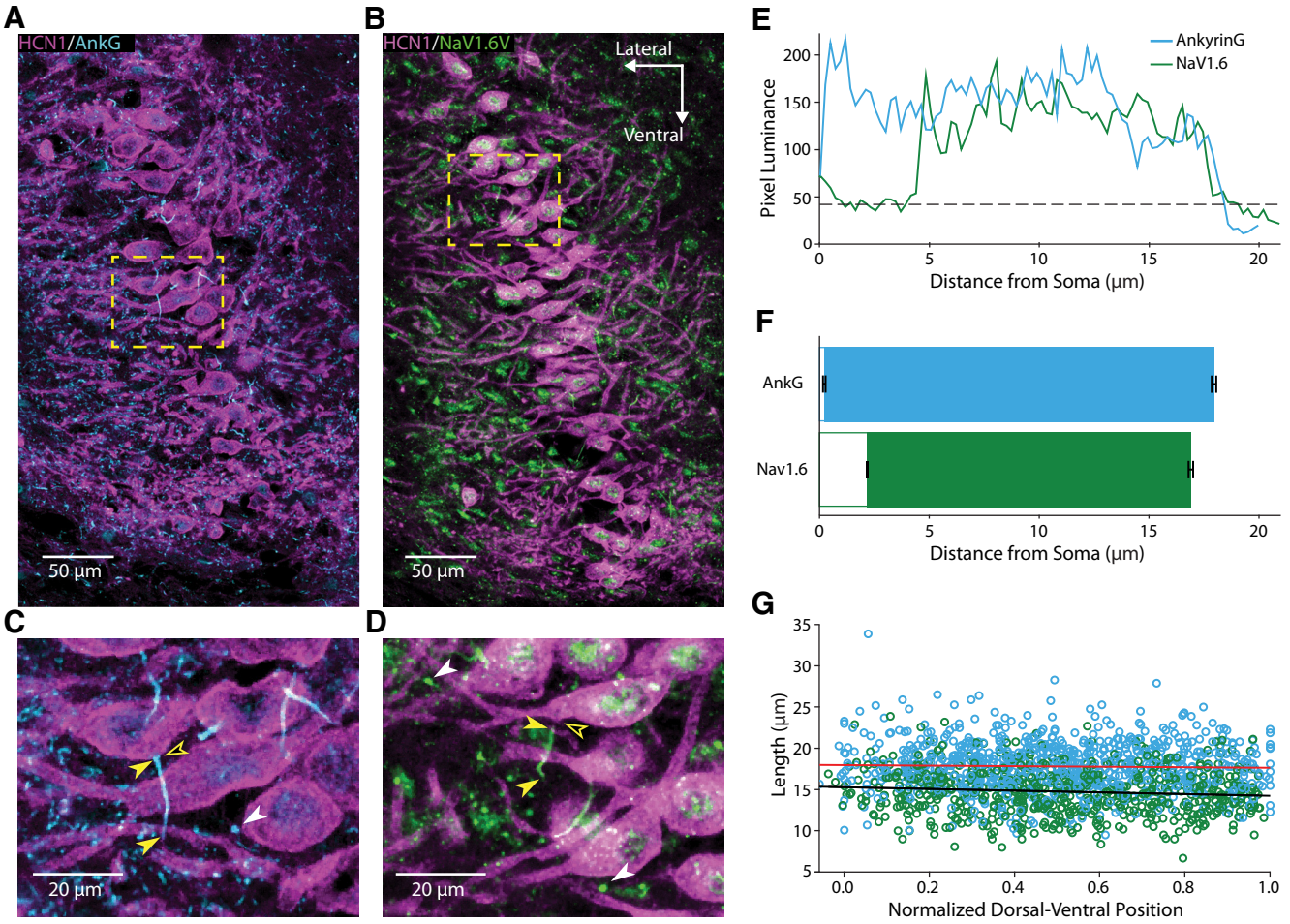

Figure 6. Axon initial segments of MSO neurons are consistent across the tonotopic axis. ***A***, ***B***, Immunostaining of coronal sections of the auditory brainstem containing the MSO for mouse anti-HCN1 (purple), and either rabbit anti-AnkyrinG (cyan) or rabbit anti-$Na_v1.6$ (green). ***C***, ***D***, Expanded regions of interest in ***A*** and ***B*** bounded by dashed yellow boxes. Open arrowheads, Presumed axonal point of emergence from the soma; filled arrowheads, proximal and distal ends of example initial segments; white arrowheads, punctate labeling indicating presumed nodes of Ranvier. ***E***, Intensity of fluorescent signal along the AIS for example neurons stained for AnkyrinG (cyan) and $Na_v1.6$ (green). The end of the AIS is defined as the point where pixel luminance dropped to <20% of the maximal signal in the tracing (dashed line). ***F***, Quantification of group data for the proximal and distal limits of the AIS (AnkyrinG signal) and $Na_v1.6$ signal. ***G***, Lengths of AnkyrinG and $Na_v1.6$ labels as a function of the tonotopic position of the neuron soma in the MSO (defined as in ***E***). Solid lines are linear fits for the AnkyrinG (red line: $y = -0.353\times + 17.895$, $R^2 = 8.9e\text{-}4$, $p = 0.39$) and $Na_v1.6$ data (black line: $y = -1.0645\times + 15.304$, $R^2 = 1.1e\text{-}2$, $p = 9.25e\text{-}3$). Data come from the following: AnkyrinG: 833 cells in 21 sections from five gerbils; $Na_v1.6$: 648 cells from 18 slices from three gerbils. All error bars represent ±SEM.

mammalian systems, gradients in membrane and firing properties can reflect tonotopic differences in HCN channels (Yamada et al., 2005; Baumann et al., 2013) and/or voltage-gated Na^+ channels (Hong et al., 2018).

Our results differ from the above studies in several important ways. There were no progressive morphologic or physiological gradients that were correlated with neuron location in the MSO. In the highest-frequency and lowest-frequency tonotopic regions, where both phasic and non-phasic firing types were found, neurons with highly disparate properties could be observed in close proximity with one another. We identified no overall systematic differences in dendritic parameters between neuron classes, despite the fact that a subset of oscillator and tonic neurons in the dorsal, low-frequency region of the MSO had unusually long dendrites (Figs. 3*A*, 4*A*). Sampling in this region was relatively sparse, and thus it is uncertain whether these unusual neurons might play a role distinct from their counterparts in the rest of the MSO neuron column. In the ventral, high-frequency region of the MSO, neurons with completely different functional properties exhibited similar dendritic morphologies, highlighting the critical role of intrinsic conductances in defining functional roles in the binaural circuit.

Mechanisms underlying physiological variation

Numerous studies have established that phasic MSO neurons exhibit extraordinarily fast membrane properties, produced primarily by high expression levels of HCN and K_v1 channels (Koch et al., 2004; Scott et al., 2005; Khurana et al., 2012). It is likely that differences in the expression levels of these channels underlie many of the differences between MSO neurons by affecting input resistance. It is important to note, however, that blockade of voltage-gated K^+ channels does not make phasic neurons fire repetitively (Scott et al., 2005), indicating a role for Na^+ currents. Phasic neurons have small, narrow APs because of the negatively shifted inactivation range of somatic voltage-gated Na^+ channels, which reduces the percentage of available Na^+ current at V_{rest} (Scott et al., 2010). Oscillator and tonic neurons have larger, faster rising APs compared with phasic neurons, likely reflecting larger Na^+ currents underlying spike generation. However, we found that AIS morphology is uniform across the

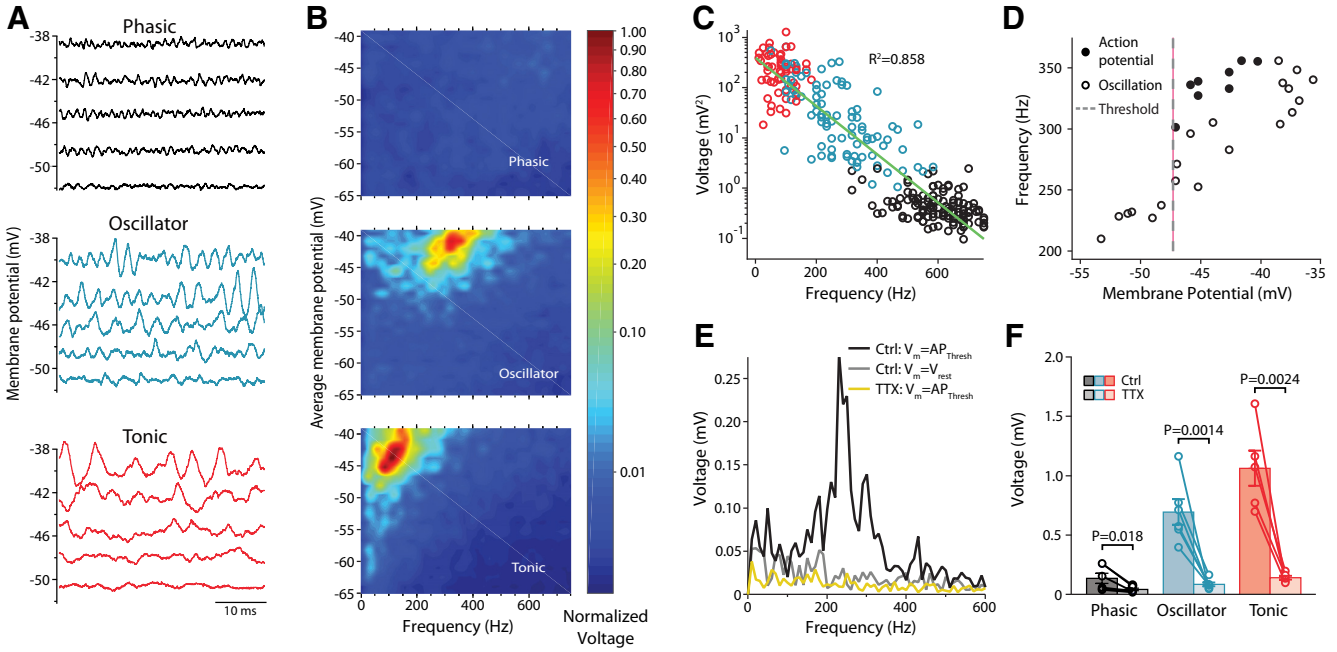

Figure 7. Oscillations are generated by the same mechanism in all firing types. ***A***, Subthreshold membrane oscillations at different voltages during subthreshold responses to current steps in MSO firing types. ***B***, Normalized voltage of oscillations in the frequency domain, derived from the FFT of traces (heatmap scale on right). Heatmaps taken from the same cells as shown in ***A***. Scale is voltage (mV^2) normalized by the peak measurement of the neuron with the largest oscillation (tonic neuron: $V(f) = 13.8\ mV^2$). ***C***, Scatterplot showing the correlation between the strongest frequency component of the oscillations of neurons and the voltage signal at that frequency. Measurements were taken from voltages 2–5 mV below spike threshold. Trendline shows the results of a linear fit to the squared voltage versus frequency relationship, $y = -0.49\times\ mV^2/Hz + 390.12\ mV^2$. ***D***, Comparison of the frequency of subthreshold oscillations (open circles) and APs (closed circles) in the same cells as a function of membrane voltage. Dashed line, Average AP threshold in MSO neurons. ***E***, Example of the FFT output of a 100 ms window from an oscillator neuron at −51 mV before (black) and after (yellow) TTX. The AP threshold was −50.3 mV in this cell. Also shown is the FFT from the voltage at rest (gray line). ***F***, Summary graph of the effects of TTX on oscillations. Transformed voltage was summed from a 100 Hz window centered around the peak frequency at a membrane potential close to threshold. *p* Values represent the results of paired, one-tailed *t* tests. All error bars represent ±SEM. Ctrl, control; Thresh, threshold.

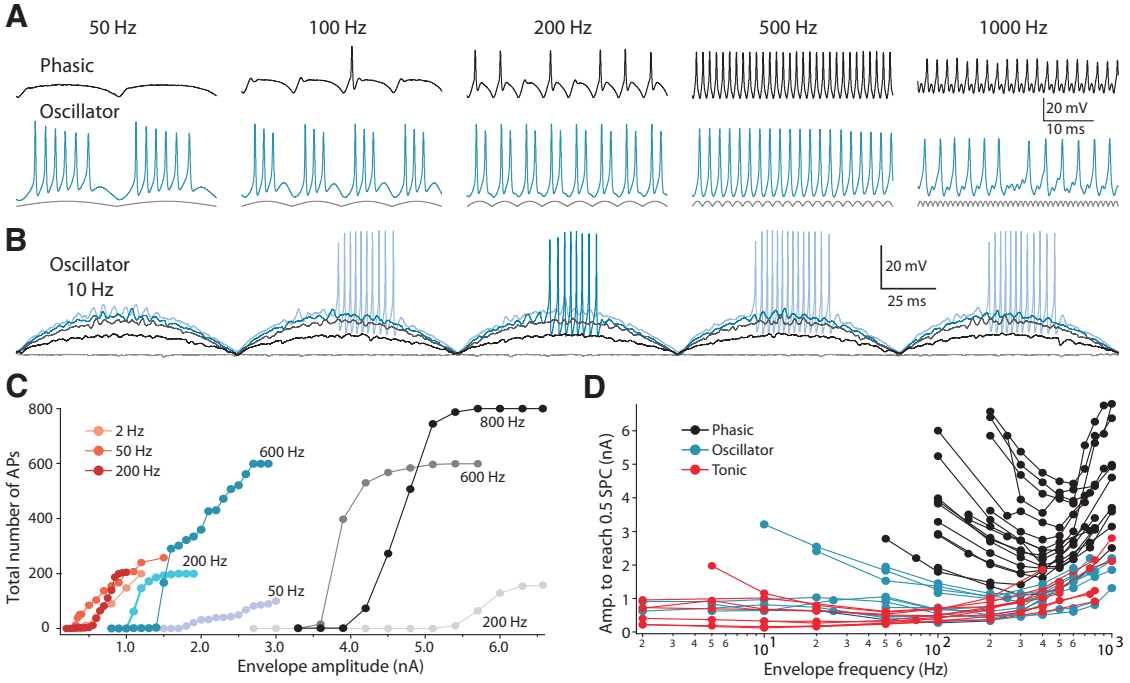

Figure 8. Envelope-like current injection reveals differential slope sensitivity of membrane voltage between cell types. ***A***, Responses of a phasic (top) and oscillator (bottom) neuron to envelope-like (rectified sine wave) current injections at different frequencies. Injected current pattern is shown in gray at the bottom. Envelope current amplitudes: phasic neuron, 2600–3000 pA; oscillator neuron, 900 pA. ***B***, Responses of an oscillator neuron to a 10 Hz envelope with peak current at 0, 500, 900, 1000, and 1100 pA. Note the increasing amplitude of subthreshold oscillations with increasing membrane voltage. ***C***, Dynamic range of firing (total spikes over 1 s envelope current injection) plotted as function of envelope amplitude. Three frequencies from each firing type are shown in different colors: phasic neuron, grayscale; oscillator, blue; tonic, red. ***D***, Envelope frequency versus the current amplitude needed to achieve an average of 0.5 spikes per cycle (SPC) at that frequency. Phasic neurons are band limited in their responses across the range of envelope frequencies, whereas oscillator and tonic neurons respond over a far broader range of frequencies.

tonotopic axis, with no increase in variance at the ventral or dorsal ends (Fig. 6). This is in contrast to findings in MNTB principal neurons (Kim et al., 2019). Thus, in the MSO, differences between firing types more likely reflects the subtype distribution, somatic expression levels, and/or modulation of voltage-gated Na^+ channels (Hu et al., 2009), rather than AIS morphology.

A surprising finding in our study is the strong influence of voltage-gated Na^+ channels in generating large, fast oscillations in MSO neurons. The resonance properties of MSO and other auditory neurons have been shown previously to amplify responses to specific frequency ranges. HCN and low voltage-activated potassium channels have been implicated as the currents responsible for producing resonance (Remme et al., 2014; Fischer et al., 2018). By contrast, the intrinsic membrane oscillations in this study were actively driven by voltage-gated Na^+ channels, and the fast-gating kinetics of the underlying currents explain why the frequency range of oscillations is higher than that of resonance frequency. We found that oscillations in nonphasic MSO neurons were of far larger amplitude and lower frequency (100–300 Hz) and could drive firing near or just above the oscillatory frequency (Figs. 7*A*,*B*, 8*D*). As with other electrophysiological parameters, the frequency of oscillations formed a continuum across the full population of MSO cells (Fig. 7*C*).

Functional implications

The extraordinary biophysical specializations that allow many MSO neurons to detect ITDs in the fine structure of sounds also prevent those neurons from reliably encoding AM and other stimuli with slow rising components (Svirskis et al., 2002; Golding and Oertel, 2012; Lehnert et al., 2014). However, *in vivo* studies in several species, including cats, guinea pigs, and gerbils, documented the ability of MSO neurons to respond to high-frequency sounds above the phase-locking range, and even to encode envelope ITDs and sinusoidal AM stimuli (Joris and Yin, 1995; Spitzer and Semple, 1995; Batra et al., 1997; Dietz et al., 2014). Furthermore, the MSO is present in many animals that do not hear low-frequency sounds, like monodelphis (Grothe and Pecka, 2014, Bazwinsky-Wutschke et al., 2016), mice (Fischl et al., 2016), and bats (Grothe et al., 1997), and the MSO of certain bat species functions to analyze aspects of AM sounds (Grothe et al., 1997; Grothe and Park, 1998). Finally, humans can detect ITDs in the low-frequency envelopes of high-frequency sounds in psychophysical experiments (McFadden and Pasanen, 1976; Nuetzel and Hafter, 1976; Bernstein and Trahiotis, 1994). The current results resolve these apparent contradictions by demonstrating that there is a subset of neurons in the MSO that is capable of responding to slow voltage changes and, potentially, envelopes. As naturalistic sounds encompass a wide diversity of acoustic waveforms, it follows that there is unlikely a clear distinction between these two modes of coding. Further, the presence of fast-rising synaptic components has been shown to influence encoding of AM-like stimuli, even in phasic neurons (Gai et al., 2010). This work contributes to a growing body of evidence blurring the lines between the supposedly parallel processing in the MSO and LSO (Joris, 1996; Franken et al., 2015, 2018), and further highlights the divergent paths of the mammalian and avian auditory system.

References

Barnes-Davies M, Barker MC, Osmani F, Forsythe ID (2004) Kv1 currents mediate a gradient of principal neuron excitability across the tonotopic axis in the rat lateral superior olive. Eur J Neurosci 19:325–333.

Batra R, Kuwada S, Fitzpatrick DC (1997) Sensitivity to interaural temporal disparities of low- and high-frequency neurons in the superior olivary complex. I. Heterogeneity of responses. J Neurophysiol 78:1222–1236.

Baumann VJ, Lehnert S, Leibold C, Koch U (2013) Tonotopic organization of the hyperpolarization-activated current (Ih) in the mammalian medial superior olive. Front Neural Circuits 7:117.

Bazwinsky-Wutschke I, Härtig W, Kretzschmar R, Rübsamen R (2016) Differential morphology of the superior olivary complex of Meriones unguiculatus and Monodelphis domestica revealed by calcium-binding proteins. Brain Struct Funct 221:4505–4523.

Bernstein LR, Trahiotis C (1994) Detection of interaural delay in high-frequency sinusoidally amplitude-modulated tones, two-tone complexes, and bands of noise. J Acoust Soc Am 95:3561–3567.

Brand A, Behrend O, Marquardt T, McAlpine D, Grothe B (2002) Precise inhibition is essential for microsecond interaural time difference coding. Nature 417:543–547.

Brew HM, Forsythe ID (2005) Systematic variation of potassium current amplitudes across the tonotopic axis of the rat medial nucleus of the trapezoid body. Hear Res 206:116–132.

Carr CE, Konishi M (1988) Axonal delay lines for time measurement in the owl's brainstem. Proc Natl Acad Sci U S A 85:8311–8315.

Carr CE, Shah S, McColgan T, Ashida G, Kuokkanen PT, Brill S, Kempter R, Wagner H (2015) Maps of interaural delay in the owl's nucleus laminaris. J Neurophysiol 114:1862–1873.

Chirila FV, Rowland KC, Thompson JM, Spirou GA (2007) Development of gerbil medial superior olive: integration of temporally delayed excitation and inhibition at physiological temperature. J Physiol 584:167–190.

Dietz M, Marquardt T, Stange A, Pecka M, Grothe B, McAlpine D (2014) Emphasis of spatial cues in the temporal fine structure during the rising segments of amplitude-modulated sounds II: single-neuron recordings. J Neurophysiol 111:1973–1985.

Fischer L, Leibold C, Felmy F (2018) Resonance properties in auditory brainstem neurons. Front Cell Neurosci 12:8.

Fischl MJ, Burger RM, Schmidt-Pauly M, Alexandrova O, Sinclair JL, Grothe B, Forsythe ID, Kopp-Scheinpflug C (2016) Physiology and anatomy of neurons in the medial superior olive of the mouse. J Neurophysiol 116:2676–2688.

Franken TP, Roberts MT, Wei L, Golding NL, Joris PX (2015) In vivo coincidence detection in mammalian sound localization generates phase delays. Nat Neurosci 18:444–452.

Franken TP, Joris PX, Smith PH (2018) Principal cells of the brainstem's interaural sound level detector are temporal differentiators rather than integrators. Elife 7:e33854.

Frisina RD, Smith RL, Chamberlain SC (1990) Encoding of amplitude modulation in the gerbil cochlear nucleus: II. Possible neural mechanisms. Hear Res 44:123–141.

Fukui I, Ohmori H (2004) Tonotopic gradients of membrane and synaptic properties for neurons of the chicken nucleus magnocellularis. J Neurosci 24:7514–7523.

Gai Y, Doiron B, Rinzel J (2010) Slope-based stochastic resonance: how noise enables phasic neurons to encode slow signals. PLoS Comput Biol 6: e1000825.

Garden DL, Dodson PD, O'Donnell C, White MD, Nolan MF (2008) Tuning of synaptic integration in the medial entorhinal cortex to the organization of grid cell firing fields. Neuron 60:875–889.

Giocomo LM, Hussaini SA, Zheng F, Kandel ER, Moser MB, Moser EI (2011) Grid cells use HCN1 channels for spatial scaling. Cell 147:1159–1170.

Goldberg JM, Brown PB (1969) Response of binaural neurons of dog superior olivary complex to dichotic tonal stimuli: some physiological mechanisms of sound localization. J Neurophysiol 32:613–636.

Golding NL, Oertel D (2012) Synaptic integration in dendrites: exceptional need for speed. J Physiol 590:5563–5569.

Grothe B, Park TJ (1998) Sensitivity to interaural time differences in the medial superior olive of a small mammal, the Mexican free-tailed bat. J Neurosci 18:6608–6622.

Grothe B, Pecka M (2014) The natural history of sound localization in mammals–a story of neuronal inhibition. Front Neural Circuits 8:116.

Grothe B, Sanes DH (1994) Synaptic inhibition influences the temporal coding properties of medial superior olivary neurons: an *in vitro* study. J Neurosci 14:1701–1709.

Grothe B, Park TJ, Schuller G (1997) Medial superior olive in the free-tailed bat: response to pure tones and amplitude-modulated tones. J Neurophysiol 77:1553–1565.

Henkel CK, Spangler KM (1983) Organization of the efferent projections of the medial superior olivary nucleus in the cat as revealed by HRP and autoradiographic tracing methods. J Comp Neurol 221:416–428.

Hong H, Wang X, Lu T, Zorio DAR, Wang Y, Sanchez JT (2018) Diverse intrinsic properties shape functional phenotype of low-frequency neurons in the auditory brainstem. Front Cell Neurosci 12:175.

Hu W, Tian C, Li T, Yang M, Hou H, Shu Y (2009) Distinct contributions of Na(v)1.6 and Na(v)1.2 in action potential initiation and backpropagation. Nat Neurosci 12:996–1002.

Jeffress LA (1948) A place theory of sound localization. J Comp Physiol Psychol 41:35–39.

Joris PX (1996) Envelope coding in the lateral superior olive. II. Characteristic delays and comparison with responses in the medial superior olive. J Neurophysiol 76:2137–2156.

Joris P, Yin TC (2007) A matter of time: internal delays in binaural processing. Trends Neurosci 30:70–78.

Joris PX, Yin TC (1995) Envelope coding in the lateral superior olive. I. Sensitivity to interaural time differences. J Neurophysiol 73:1043–1062.

Karino S, Smith PH, Yin TC, Joris PX (2011) Axonal branching patterns as sources of delay in the mammalian auditory brainstem: a re-examination. J Neurosci 31:3016–3031.

Khurana S, Remme MW, Rinzel J, Golding NL (2011) Dynamic interaction of I_h and IK-LVA during trains of synaptic potentials in principal neurons of the medial superior olive. J Neurosci 31:8936–8947.

Khurana S, Liu Z, Lewis AS, Rosa K, Chetkovich D, Golding NL (2012) An essential role for modulation of hyperpolarization-activated current in the development of binaural temporal precision. J Neurosci 32:2814–2823.

Kim EJ, Feng C, Santamaria F, Kim JH (2019) Impact of auditory experience on the structural plasticity of the AIS in the mouse brainstem throughout the lifespan. Front Cell Neurosci 13:456.

Ko KW, Rasband MN, Meseguer V, Kramer RH, Golding NL (2016) Serotonin modulates spike probability in the axon initial segment through HCN channels. Nat Neurosci 19:826–834.

Koch U, Braun M, Kapfer C, Grothe B (2004) Distribution of HCN1 and HCN2 in rat auditory brainstem nuclei. Eur J Neurosci 20:79–91.

Koppl C (1994) Auditory nerve terminals in the cochlear nucleus magnocellularis: differences between low and high frequencies. J Comp Neurol 339:438–446.

Kuba H (2012) Structural tuning and plasticity of the axon initial segment in auditory neurons. J Physiol 590:5571–5579.

Kuba H, Yamada R, Fukui I, Ohmori H (2005) Tonotopic specialization of auditory coincidence detection in nucleus laminaris of the chick. J Neurosci 25:1924–1934.

Lehnert S, Ford MC, Alexandrova O, Hellmundt F, Felmy F, Grothe B, Leibold C (2014) Action potential generation in an anatomically constrained model of medial superior olive axons. J Neurosci 34:5370–5384.

Mathews PJ, Jercog PE, Rinzel J, Scott LL, Golding NL (2010) Control of submillisecond synaptic timing in binaural coincidence detectors by K(v)1 channels. Nat Neurosci 13:601–609.

McFadden D, Pasanen EG (1976) Lateralization of high frequencies based on interaural time differences. J Acoust Soc Am 59:634–639.

Nuetzel JM, Hafter ER (1976) Lateralization of complex waveforms: effects of fine structure, amplitude, and duration. J Acoust Soc Am 60:1339–1346.

Padmanabhan K, Urban NN (2010) Intrinsic biophysical diversity decorrelates neuronal firing while increasing information content. Nat Neurosci 13:1276–1282.

Rautenberg PL, Grothe B, Felmy F (2009) Quantification of the three-dimensional morphology of coincidence detector neurons in the medial superior olive of gerbils during late postnatal development. J Comp Neurol 517:385–396.

Remme MW, Donato R, Mikiel-Hunter J, Ballestero JA, Foster S, Rinzel J, McAlpine D (2014) Subthreshold resonance properties contribute to the efficient coding of auditory spatial cues. Proc Natl Acad Sci U S A 111:E2339–2348.

Roberts MT, Seeman SC, Golding NL (2013) A mechanistic understanding of the role of feedforward inhibition in the mammalian sound localization circuitry. Neuron 78:923–935.

Roberts RC, Ribak CE (1987) GABAergic neurons and axon terminals in the brainstem auditory nuclei of the gerbil. J Comp Neurol 258:267–280.

Sanes DH, Goldstein NA, Ostad M, Hillman DE (1990) Dendritic morphology of central auditory neurons correlates with their tonotopic position. J Comp Neurol 294:443–454.

Scheibel ME, Scheibel AB (1974) Neuropil organization in the superior olive of the cat. Exp Neurol 43:339–348.

Scott LL, Mathews PJ, Golding NL (2005) Posthearing developmental refinement of temporal processing in principal neurons of the medial superior olive. J Neurosci 25:7887–7895.

Scott LL, Hage TA, Golding NL (2007) Weak action potential backpropagation is associated with high-frequency axonal firing capability in principal neurons of the gerbil medial superior olive. J Physiol 583:647–661.

Scott LL, Mathews PJ, Golding NL (2010) Perisomatic voltage-gated sodium channels actively maintain linear synaptic integration in principal neurons of the medial superior olive. J Neurosci 30:2039–2050.

Smith PH (1995) Structural and functional differences distinguish principal from nonprincipal cells in the guinea pig MSO slice. J Neurophysiol 73:1653–1667.

Smith DJ, Rubel EW (1979) Organization and development of brain stem auditory nuclei of the chicken: dendritic gradients in nucleus laminaris. J Comp Neurol 186:213–239.

Spitzer MW, Semple MN (1995) Neurons sensitive to interaural phase disparity in gerbil superior olive: diverse monaural and temporal response properties. J Neurophysiol 73:1668–1690.

Stotler WA (1953) An experimental study of the cells and connections of the superior olivary complex of the cat. J Comp Neurol 98:401–431.

Svirskis G, Kotak V, Sanes DH, Rinzel J (2002) Enhancement of signal-to-noise ratio and phase locking for small inputs by a low-threshold outward current in auditory neurons. J Neurosci 22:11019–11025.

Tripathy SJ, Padmanabhan K, Gerkin RC, Urban NN (2013) Intermediate intrinsic diversity enhances neural population coding. Proc Natl Acad Sci U S A 110:8248–8253.

van Buuren S, Groothuis-Oudshoorn K (2011) Multivariate imputation by chained equations in R. J Stat Soft 45:1–67.

Wang X, Hong H, Brown DH, Sanchez JT, Wang Y (2017) Distinct neural properties in the low-frequency region of the chicken cochlear nucleus magnocellularis. eNeuro 4:ENEURO.0016-17.2017.

Wenthold RJ, Huie D, Altschuler RA, Reeks KA (1987) Glycine immunoreactivity localized in the cochlear nucleus and superior olivary complex. Neuroscience 22:897–912.

Yamada R, Kuba H, Ishii TM, Ohmori H (2005) Hyperpolarization-activated cyclic nucleotide-gated cation channels regulate auditory coincidence detection in nucleus laminaris of the chick. J Neurosci 25:8867–8877.

Yin TC, Chan JC (1990) Interaural time sensitivity in medial superior olive of cat. J Neurophysiol 64:465–488.